

PAPER • OPEN ACCESS

$\text{La}_2\text{Rh}_{3+\delta}\text{Sb}_4$: a new ternary superconducting rhodium-antimonide

To cite this article: Kangqiao Cheng *et al* 2022 *Mater. Futures* 1 045201

View the [article online](#) for updates and enhancements.

You may also like

- [Tunable crystallization mechanism of \$\text{Sb}_4\text{Te}\$ films by \$\text{VO}_x\$ nano-grid framework for breaking through the trade-off between thermal stability and crystallization speed](#)
Yang Li and Yegang Lu
- [Vertical strain-induced modification of the electrical and spin properties of monolayer \$\text{MoSi}_2\text{X}_4\$ \(\$X = \text{N}, \text{P}, \text{As}\$ and \$\text{Sb}\$ \)](#)
Shoeib Babaei Touski and Nayereh Ghobadi
- [Metal-inorganic frameworks with pnictogen linkers](#)
Tatiana A. Shestimerova and Andrei V. Shevelkov

La₂Rh_{3+ δ} Sb₄: a new ternary superconducting rhodium-antimonide

Kangqiao Cheng^{1,5}, Wei Xie^{1,5}, Shuo Zou¹, Huanpeng Bu², Jin-Ke Bao³, Zengwei Zhu¹, Hanjie Guo^{2,*}, Chao Cao^{4,*} and Yongkang Luo^{1,*} 

¹ Wuhan National High Magnetic Field Center and School of Physics, Huazhong University of Science and Technology, Wuhan 430074, People's Republic of China

² Neutron Science Platform, Songshan Lake Materials Laboratory, Dongguan, Guangdong 523808, People's Republic of China

³ Department of Physics, Materials Genome Institute and International Center for Quantum and Molecular Structures, Shanghai University, Shanghai 200444, People's Republic of China

⁴ Center for Correlated Matter and School of Physics, Zhejiang University, Hangzhou 310058, People's Republic of China

E-mail: hjguo@sslabor.org.cn, ccao@zju.edu.cn and mpzlyk@gmail.com

Received 18 August 2022, revised 28 September 2022

Accepted for publication 2 October 2022

Published 17 October 2022



CrossMark

Abstract

Rhodium-containing compounds offer a fertile playground to explore novel materials with superconductivity (SC) and other fantastic electronic correlation effects. A new ternary rhodium-antimonide La₂Rh_{3+ δ} Sb₄ ($\delta \approx 1/8$) has been synthesized by a Bi-flux method. It crystallizes in the orthorhombic Pr₂Ir₃Sb₄-like structure, with the space group *Pnma* (No. 62). The crystalline structure appears as stacking the two-dimensional RhSb₄- and RhSb₅-polyhedra networks along **b** axis, and the La atoms embed in the cavities of these networks. Band structure calculations confirm it as a multi-band metal with a van-Hove singularity like feature at the Fermi level, whose density of states are mainly of Rh-4*d* and Sb-5*p* characters. The calculations also imply that the redundant Rh acts as charge dopant. SC is observed in this material with onset transition at $T_c^{\text{on}} \approx 0.8$ K. Ultra-low temperature magnetic susceptibility and specific heat measurements suggest that it is an *s*-wave type-II superconductor. Our work may also imply that the broad Ln₂Tm_{3+ δ} Sb₄ (Ln = rare earth, Tm = Rh, Ir) family may host new material bases where new superconductors, quantum magnetism and other electronic correlation effects could be found.

Supplementary material for this article is available [online](#)

Keywords: superconductivity, electronic correlation effect, crystalline structure

1. Introduction

Ternary rhodium-containing compounds have spanned fertile material bases for studies of unconventional superconductivity

(SC) and electronic correlation effects. On the one hand, Rh-4*d* electrons possess moderate on-site Coulomb repulsion *U* and spin-orbit coupling (SOC) strength, which endow them with variable—either localized or itinerant—electronic states (e.g. see [1, 2]). On the other hand, the orbital configuration 4*d*⁸5*s*¹ of Rh may lead to a large density of states (DOS) in the presence of specific crystalline electric field, which enhances inter-site hybridization and in turn facilitates rich physical properties such as heavy-fermion SC observed in CeRh₂Si₂ [3], CeRhIn₅ [4], PuRhGa₅ [5], URhGe [6] and CeRh₂As₂ [7, 8], Kondo insulator in CeRh(As,Sb) [9], unconventional

⁵ These authors contribute equally to this work.

* Authors to whom any correspondence should be addressed.



Original Content from this work may be used under the terms of the [Creative Commons Attribution 4.0 licence](#). Any further distribution of this work must maintain attribution to the author(s) and the title of the work, journal citation and DOI.

Future perspectives

The moderate on-site Coulomb repulsion U and SOC strength of Rh-4d electrons endow them with variable, intriguing natures, and this offers a rich platform for materials design. We hereby report a new ternary rhodium-containing compound $\text{La}_2\text{Rh}_{3+\delta}\text{Sb}_4$ ($\delta \approx 1/8$) that becomes a type-II superconductor at low temperature. More importantly, our work also suggests that the broad family of $\text{Ln}_2\text{Tm}_{3+\delta}\text{Sb}_4$ (Ln = rare earth, Tm = transition metals)—whose physical properties are not yet well explored—likely hosts new quantum material bases where novel SC, quantum magnetism, quantum criticality and other electronic correlation effects can be found.

quantum criticality in YbRh_2Si_2 [10] and CeRh_6Ge_4 [11], and quadrupolar Kondo effect in $\text{PrRh}_2\text{Zn}_{20}$ [12].

The chemical formula $\text{LnTm}_{2-x}\text{Pn}_2$ (Ln = rare earth, Tm = transition metal, Pn = P, As, Sb) stands for a big class of ternary pnictides that attracted a broad audience in recent years. Amongst them, the most well-known phases should be the so-called ‘122’ family ($x=0$) that consists of two branches of tetragonal crystalline structures: the ThCr_2Si_2 type ($I4/mmm$, No. 139) and CaBe_2Ge_2 type ($P4/nmm$, No. 129). Besides these stoichiometric 122 phases, substantial deficient can exist on the transition metal site [13–16]. It is interesting to note that in some cases, such deficient can maintain the 122-type structure, e.g. $\text{CeNi}_{1.75}\text{As}_2$ [17], while in other cases, the structure collapses and changes into a new structure. A representative example is $\text{Pr}_2\text{Ir}_3\text{Sb}_4$ ($x=1$) which belongs to the orthorhombic $Pnma$ space group (No. 62). Multiple compounds have been found to crystallize in this 234 phase, such as $\text{Ln}_2\text{Ir}_3\text{Sb}_4$ (Ln = La, Ce, Pr, Nd) [18] and $\text{Ce}_2\text{Rh}_3\text{Sb}_4$ [19]. In particular, previous studies on the rhodium-antimonide $\text{Ce}_2\text{Rh}_3\text{Sb}_4$ based on polycrystal samples manifested that the local moments of Ce^{3+} remain paramagnetic down to 2 K [19], implying that it probably sits nearby a quantum critical point. Single crystals with high quality are needed to better understand its ground state.

With the goal of growing the single crystalline $\text{Ce}_2\text{Rh}_3\text{Sb}_4$ and its non-4f reference, we discovered a new ternary rhodium-antimonide $\text{La}_2\text{Rh}_{3+\delta}\text{Sb}_4$ that crystallizes in the orthorhombic $\text{Pr}_2\text{Ir}_3\text{Sb}_4$ -like structure with redundant Rh. Herein, we report the synthesis of $\text{La}_2\text{Rh}_{3+\delta}\text{Sb}_4$ single crystals, determination of its crystalline structure, and systematic study of its physical properties by a combination of electrical transport/magnetic/thermodynamic measurements and first-principles band structure calculations. Our work reveals that $\text{La}_2\text{Rh}_{3+\delta}\text{Sb}_4$ is a new superconducting material with onset temperature $T_c^{\text{on}} \approx 0.8$ K, and its normal state is a multi-band metal with van-Hove singularity like feature at the Fermi level.

2. Experimental

Single crystals of $\text{La}_2\text{Rh}_{3+\delta}\text{Sb}_4$ were synthesized by a Bi-flux method. La chunk (Alfa Aesar, 99.9%), Rh powder (Aladdin, 99.95%), Sb granule (Aladdin, 99.9999%), and Bi granule (Aladdin, 99.9999%) were weighed in a molar ratio of 2:3:4:40. The mixture was transferred into an alumina crucible

which was sealed in an evacuated quartz tube. All these operations were conducted in an argon-filled glove box to avoid the contamination of water and oxygen. The quartz tube was heated to 500 °C in 20 h and held for one day. Then, it was raised to 1100 °C in 30 h and sintered at this temperature for 100 h. After that, in two weeks it was slowly cooled down to 500 °C at which temperature the Bi-flux was removed by centrifugation. The remaining Bi flux can be dissolved by a mixture of an equal volume of hydrogen peroxide and acetic acid. The obtained samples were needle-like with typical dimensions $\sim 4 \times 0.5 \times 0.3$ mm³ (see figure 1(a)), and are stable in air and moisture. The same method is also applicable to grow the $\text{Ce}_2\text{Rh}_{3+\delta}\text{Sb}_4$ single crystals, a heavy-fermion compound whose low-temperature physical properties will be published elsewhere [20].

The chemical composition of the new compound was verified by energy dispersive x-ray spectroscopy (EDS) affiliated to a field emission scanning electron microscope (FEI Model SIRION), which gives the atomic ratio La:Rh:Sb = 22.2(9):33.2(4):44.7(6), close to the stoichiometric $\text{La}_2\text{Rh}_3\text{Sb}_4$, as shown in supplementary information (SI). The crystalline structure of the compound was determined by a Rigaku XtaLAB mini II single crystal x-ray diffractometer (XRD) with Mo radiation ($\lambda_{K\alpha} = 0.71073$ Å). Several single crystals were selected to collect diffraction data for structural refinement. We used the olex2-1.5 software of SHELX-2018 package and full-matrix least squares on the F^2 model to perform the refinement. The cell parameters and atomic coordinates were all determined, and the qualified CIF report was generated (SI). Scanning transmission electron microscope (STEM) images were recorded at 300 kV using a probe Cs-corrected Spectra 300 (Thermo Fisher Ltd) in both dark-field (DF) and high-angle annular dark-field (HAADF) modes. Cross-section TEM sample was prepared on the [0 1 0] plane using Helios 5UX 30 kV Ga focused ion beam.

A Magnetic Property Measurement System (SQUID-VSM, Quantum Design) was employed to measure the DC magnetic susceptibility between 1.8 and 300 K in the presence of external field 1000 Oe ($\mathbf{H} \perp \mathbf{b}$). Electrical resistivity was measured in a standard four-probe method with current parallel to \mathbf{b} axis, in a Physical Property Measurement System (PPMS-9, Quantum Design). The same instrument was also used for the specific heat measurements. For sub-Kelvin experiments, a dilution refrigerator insert was utilized to measure resistivity, AC susceptibility and specific heat. The AC susceptibility was measured at zero static magnetic field with AC driving field 0.5 Oe and various frequencies.

The electronic band structure and DOS were calculated on the stoichiometric $\text{La}_2\text{Rh}_3\text{Sb}_4$ using density-functional theory (DFT) method as implemented in Vienna *Ab initio* Simulation Package [21]. The plane-wave basis up to 400 eV and Perdew–Burke–Ernzerhoff (PBE) [22] flavor of generalized gradient approximation to exchange–correlation functional were employed. The ion–valence electron interaction were approximated with projected augmented wave method [23, 24]. SOC was considered in all calculations. A $3 \times 12 \times 4$ Monkhorst–Pack K-grid for Brillouin zone integration was found to converge the total energy within 1 meV/atom.

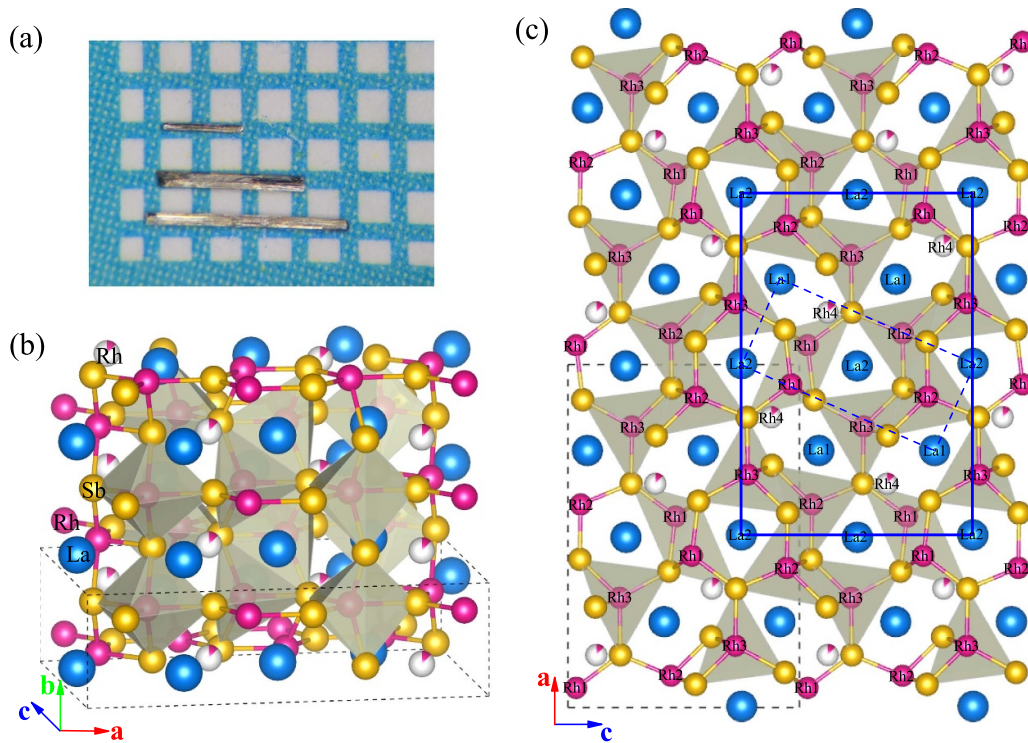


Figure 1. (a) A photograph of $\text{La}_2\text{Rh}_{3+\delta}\text{Sb}_4$ single crystals on millimeter-grid paper. The single crystals are needle-like along \mathbf{b} axis. Figures (b)–(c) show the crystalline structure. The partially occupied Rh4 is double-colored. The black-dotted rectangles mean the original unit cell as determined by XRD refinement. To better compare the crystalline structure to the STEM image, a translated unit cell is also shown by the blue-solid rectangle. The blue-dashed rectangular shows the part that mimics the distorted CaBe_2Ge_2 -type structure.

Using the experimental structure as initial guess, the crystal geometry was fully optimized until forces on each atom less than $1 \text{ meV } \text{Å}^{-1}$ and internal stress less than 1 kBar.

3. Results and discussion

3.1. Crystalline structure

Figure 1(b) shows the crystal structure of $\text{La}_2\text{Rh}_{3+\delta}\text{Sb}_4$. It is of the orthorhombic $\text{Pr}_2\text{Ir}_3\text{Sb}_4$ -like structure [18, 19], in the space group $Pnma$ (No. 62). During the structural refinement, we were aware of some redundant electron density near the site (0.3471, 0.25, 0.6223), and this was later recognized as the Rh4 site that has a partial occupation rate $\sim 0.122(4)$, by STEM experiments (see below). The refined lattice parameters are $a = 16.2667(5) \text{ Å}$, $b = 4.5858(2) \text{ Å}$, $c = 11.0068(4) \text{ Å}$, $\alpha = \beta = \gamma = 90^\circ$, and $Z = 4$. The density of this material is 8.787 g cm^{-3} . More details about the structural information can be found in table 1, while the atomic coordination and anisotropic displacement parameters are listed in tables 2 and S1, respectively. The refinement results for R_1 and wR_2 are 0.0286 and 0.0560, respectively, confirming the validity of XRD refinement. It can be seen from the analysis that the structure we derived is essentially isomorphic with $\text{Ce}_2\text{Rh}_3\text{Sb}_4$ that was reported previously by polycrystal studies [18, 19]. As expected, the lattice parameters a , b , and c of $\text{Ce}_2\text{Rh}_3\text{Sb}_4$ are relatively smaller than in $\text{La}_2\text{Rh}_{3+\delta}\text{Sb}_4$ [19], owing to the lanthanide contraction effect.

Table 1. Single-crystal XRD refinement data for $\text{La}_2\text{Rh}_{3+\delta}\text{Sb}_4$ at 290 K.

Composition	$\text{La}_2\text{Rh}_{3+\delta}\text{Sb}_4$
Formula weight (g mol^{-1})	1086.16
Space group	$Pnma$ (No. 62)
a (Å)	16.2667(5)
b (Å)	4.5858(2)
c (Å)	11.0068(4)
V (Å ³)	821.06(5)
Z	4
ρ (g cm^{-3})	8.787
2θ range	4.468° – 51.998°
No. of reflections, R_{int}	3112, 0.0307
No. of independent reflections	916
No. of parameters	62
R_1^a , wR_2^b [$I > 2\delta(I)$]	0.0250, 0.0545
R_1 , wR_2 (all data)	0.0286, 0.0560
Goodness of fit on F^2	1.135
Largest diffraction peak and hole ($\text{e } \text{Å}^{-3}$)	1.92 and -1.90

$$^a R_1 = \sum ||F_{\text{obs}}| - |F_{\text{cal}}|| / \sum |F_{\text{obs}}|$$

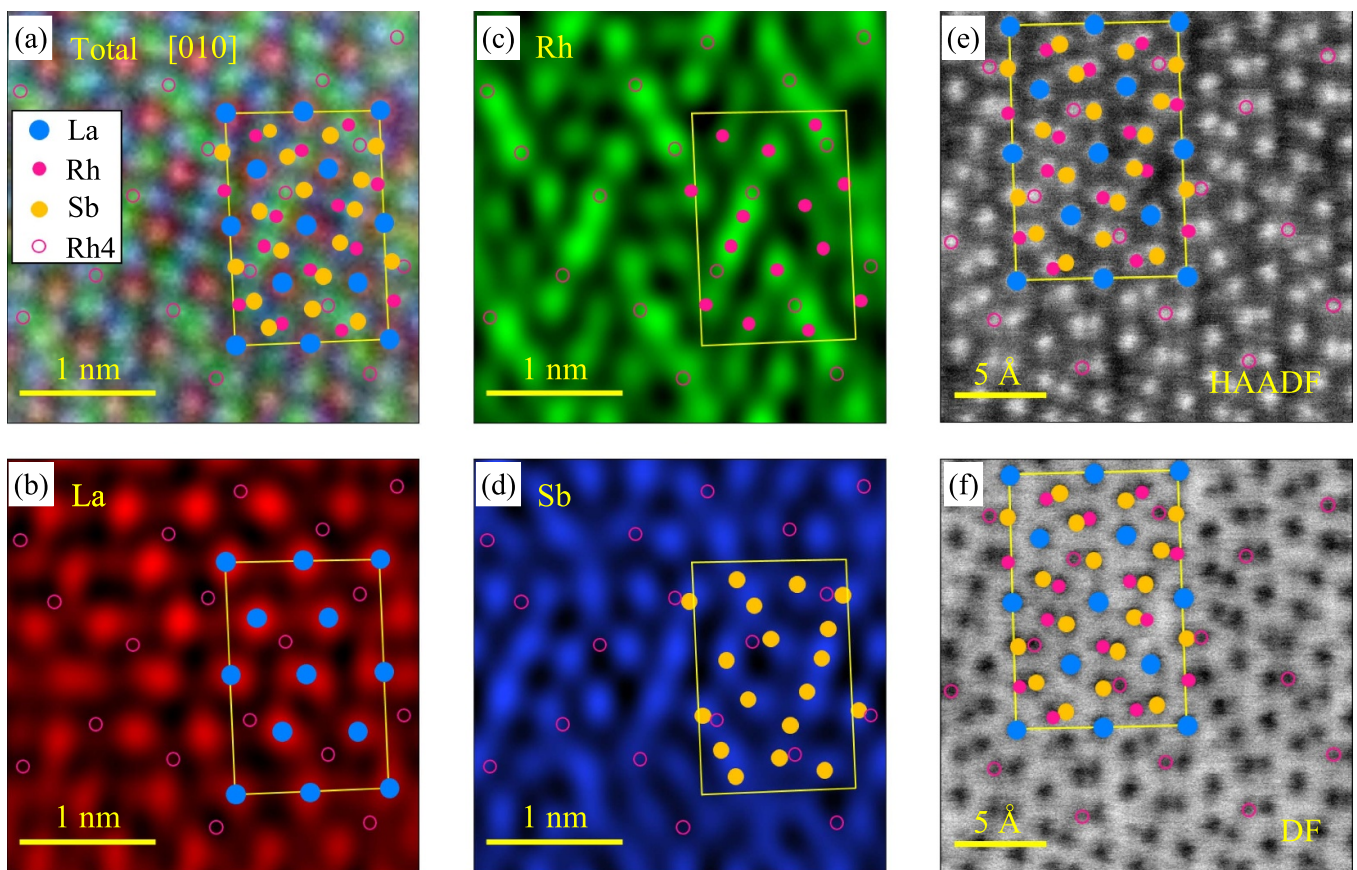
$$^b wR_2 = [\sum w(F_{\text{obs}}^2 - F_{\text{cal}}^2)^2 / \sum w(F_{\text{obs}}^2)^2]^{1/2}$$

$$w = 1/[\sigma^2 F_{\text{obs}}^2 + (a \cdot P)^2 + b \cdot P], \text{ where } P = [\max(F_{\text{obs}}^2) + 2F_{\text{cal}}^2]/3.$$

To clarify more details about the crystalline phase, we performed STEM measurements, as shown in figure 2. The high spatial resolution enables us to view individual atoms in the [0 1 0] plane, and the coordinates of the atoms are in good agreement with XRD refinement. We then project the Rh4

Table 2. Structural parameters and equivalent isotropic displacement parameters U_{eq} of $\text{La}_2\text{Rh}_{3+\delta}\text{Sb}_4$. U_{eq} is taken as 1/3 of the trace of the orthogonalized U_{ij} tensor.

Atoms	Wyck.	x	y	z	Occ.	U_{eq} (\AA^2)
La1	4c	0.249 98(4)	0.2500	0.915 87(7)	1.000	0.0057(2)
La2	4c	0.503 41(4)	0.2500	0.749 38(6)	1.000	0.0080(2)
Sb1	4c	0.432 60(4)	0.2500	0.051 18(7)	1.000	0.0053(2)
Sb2	4c	0.653 45(4)	0.2500	0.273 33(7)	1.000	0.0067(2)
Sb3	4c	0.293 35(5)	0.7500	0.118 40(7)	1.000	0.0082(2)
Sb4	4c	0.397 86(4)	0.2500	0.436 16(7)	1.000	0.0091(2)
Rh1	4c	0.557 19(5)	0.2500	0.464 57(8)	1.000	0.0033(2)
Rh2	4c	0.592 33(5)	0.2500	0.054 55(8)	1.000	0.0039(2)
Rh3	4c	0.320 15(5)	0.2500	0.223 21(8)	1.000	0.0055(2)
Rh4	4c	0.3471(5)	0.2500	0.6223(7)	0.122(4)	0.0163(2)

**Figure 2.** STEM images of $\text{La}_2\text{Rh}_{3+\delta}\text{Sb}_4$ on $[0\ 1\ 0]$ plane. STEM-EDS elemental maps respectively for (a) total, (b) La, (c) Rh, and (d) Sb. The atomic coordinates in a unit cell of $\text{La}_2\text{Rh}_{3+\delta}\text{Sb}_4$ are projected to the images. The filled blue, pink and green circles are La, Rh(1–3) and Sb atoms, respectively, while the open pink circles represent the occupied Rh4 sites. (e) HAADF image. (f) DF image.

coordinates onto the STEM-EDS elemental maps for La, Rh, and Sb (figures 2(b)–(d)) respectively), and noticed that they fit only to the Rh image satisfactorily well, cf the open pink circles in figure 2(c), confirming the occupation of Rh atoms at these sites. In general, the contrast at Rh4 sites is relatively lower (figures 2(e) and (f)), because of the partial occupation. Note that the STEM sample is tens of nanometers in thickness which contains an order of magnitude 10–100 layers. Further studies based on first-principles calculations suggest that Rh4 likely serves as charge dopant, seeing below.

On the whole, the crystalline structure of $\text{La}_2\text{Rh}_{3+\delta}\text{Sb}_4$ can be viewed as stacking the Rh–Sb polyhedron networks along the \mathbf{b} axis, and the La and Rh4 atoms reside inside the cavities of these networks (figure 1(c)). The local environments for Rh1, Rh2 and Rh3 are depicted in figure 3. Rh1 is surrounded by one Sb2 and three Sb4, forming a distorted tetrahedron. Rh2 has five near-neighbor Sb atoms: three Sb1, one Sb2 and one Sb3, and they construct a hexahedron. The situation for Rh3 is similar, i.e. one Sb1, one Sb2, two Sb3 and one Sb4 also build up a hexahedron; however, here the Sb1, Sb2 and two

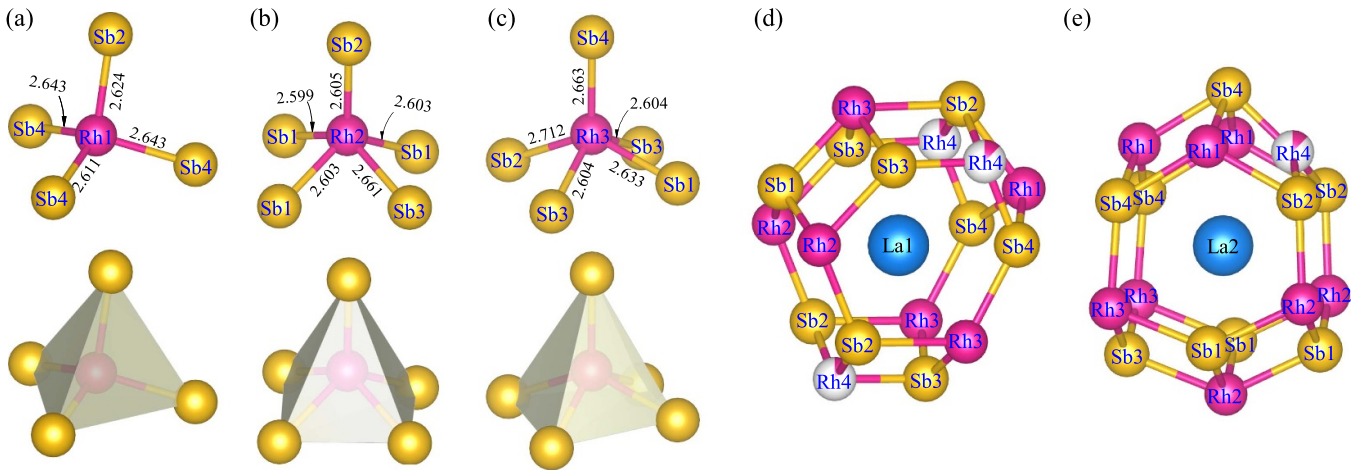


Figure 3. Local environments in $\text{La}_2\text{Rh}_{3+\delta}\text{Sb}_4$, (a) for Rh1, (b) for Rh2, (c) for Rh3, (d) for La1, and (e) for La2. The bond lengths are in Å.

Sb3 atoms are almost in the same plane, so the hexahedron looks rather like a pyramid. The interatomic distances for Rh–Sb bondings are shown in figure 2. Viewing along the **b** axis (figure 1(c)), one clearly finds that two edge-sharing Rh1 tetrahedra are connected to two Rh2 and four Rh3 hexahedra by corner-sharing, of which each Rh2 hexahedron connects to one other Rh2 and Rh3 hexahedra by edge-sharing, while each Rh3 hexahedra connects to two other Rh2 hexahedra by edge-sharing and corner-sharing. In this way, a two-dimensional Rh–Sb polyhedron network is weaved in the **ac**-plane, and two kinds of cavities come into being: a quadrilateral type filled with La1 and Rh4, and a triangular type filled with La2. See more details in figure 1(c).

From the viewpoint of La, both La1 and La2 are surrounded by 18 Rh and Sb sites (including Rh4), seeing figures 3(d) and (e). These coordination numbers reduce to 15 and 17 respectively in the standard $\text{Pr}_2\text{Ir}_3\text{Sb}_4$ structure. Noteworthy that the local coordination for La2 mimics that of Ca in the CaBe_2Ge_2 -type 122 phase, therefore, part of the structure that resembles a distorted CaBe_2Ge_2 can be recognized in $\text{La}_2\text{Rh}_{3+\delta}\text{Sb}_4$, as shown by the blue-dashed rectangular in figure 1(c). A clearer description can be found in [19].

3.2. Physical properties

Figure 4(a) displays the temperature dependence of resistivity for electric current along **b**. At room temperature, $\rho_b = 79.6 \mu\Omega\text{cm}$. Upon cooling, $\rho_b(T)$ decreases almost linearly until for $T < 50$ K a Fermi liquid behavior $\rho_b = \rho_0 + AT^2$ can be well fit to the data, where the prefactor $A = 2.17 \times 10^{-3} \mu\Omega\text{cm K}^{-2}$, and $\rho_0 = 43.6 \mu\Omega\text{cm}$ stands for residual resistivity. This fit also yields the residual resistivity ratio $\text{RRR} \equiv \rho(300\text{K})/\rho_0 = 1.8$. The low RRR is likely due to disorders introduced by the partially occupied Rh4. Further decreasing temperature in a dilution refrigerator, we find ρ_b drops rapidly below $T_c^{\text{on}} \approx 0.8$ K and essentially vanishes at $T_c^0 = 0.65$ K, indicating a SC transition. The onset of SC,

T_c^{on} , is determined at which temperature ρ_b drops to 99% of $\rho_b(1\text{K})$, seeing the inset to figure 4(a).

Next, we took the resistivity measurements under magnetic field **H** perpendicular to and parallel with **b**, and the results are displayed in figures 4(b) and (c), respectively. For **H** \perp **b**, magnetic field gradually suppresses the SC transition, and when $\mu_0 H = 0.12$ T, seldom resistivity drop can be seen. The upper critical field $\mu_0 H_{c2}(0)$ can be obtained from the $\rho_b(H, T)$ data, by fitting the field dependent T_c^{on} to the Ginzburg–Landau formula [25], $\mu_0 H_{c2}(T) = \mu_0 H_{c2}(0)(1 - t^2)/(1 + t^2)$, where $t = T/T_c^{\text{on}}$ is the reduced temperature. This fit results in $\mu_0 H_{c2}^{\perp b}(0) = 0.13$ T. The measurements for **H** \parallel **b** were made on another sample whose SC transition is similar. In this field orientation, we derived $\mu_0 H_{c2}^{\parallel b}(0) = 0.26$ T. The anisotropy of upper critical field thus is ~ 2 . These $\mu_0 H_{c2}$ values are far less than the Pauli paramagnetic limit $\mu_0 H_P = 1.84T_c \approx 1.4$ T [26, 27], implying that orbital limiting is the dominant.

The SC of $\text{La}_2\text{Rh}_{3+\delta}\text{Sb}_4$ is further confirmed by magnetic shielding effect, as shown in figure 5. Our DC magnetic susceptibility results reveal a weak paramagnetic property above 2 K, characteristic of itinerant metals with little local moment. Note that the upturn tail at low temperature is probably due to a tiny amount of magnetic impurity. AC susceptibility was employed for the sub-Kelvin region. The real part of AC susceptibility χ' drops rapidly below 0.65 K and the crystal becomes diamagnetic. We should point out that the transition temperature determined by $\chi'(T)$ is very close to T_c^0 from resistivity measurements, manifesting that bulk SC is realized below 0.65 K. Far below T_c , the magnetic shielding fraction of SC (without taking demagnetization-factor correction) exceeds 400% (cf upper inset to figure 5). Furthermore, we also notice that the SC transition is frequency dependent, i.e. the peak of $\chi''(T)$, the imaginary part of AC susceptibility, moves to higher temperature as the frequency increases. This is reminiscent of dissipation caused by flux motion in the mixed state of SC, and implies that $\text{La}_2\text{Rh}_{3+\delta}\text{Sb}_4$ is a type-II superconductor.

To further study the SC properties of $\text{La}_2\text{Rh}_{3+\delta}\text{Sb}_4$, we turn to specific heat measurements, the results of which

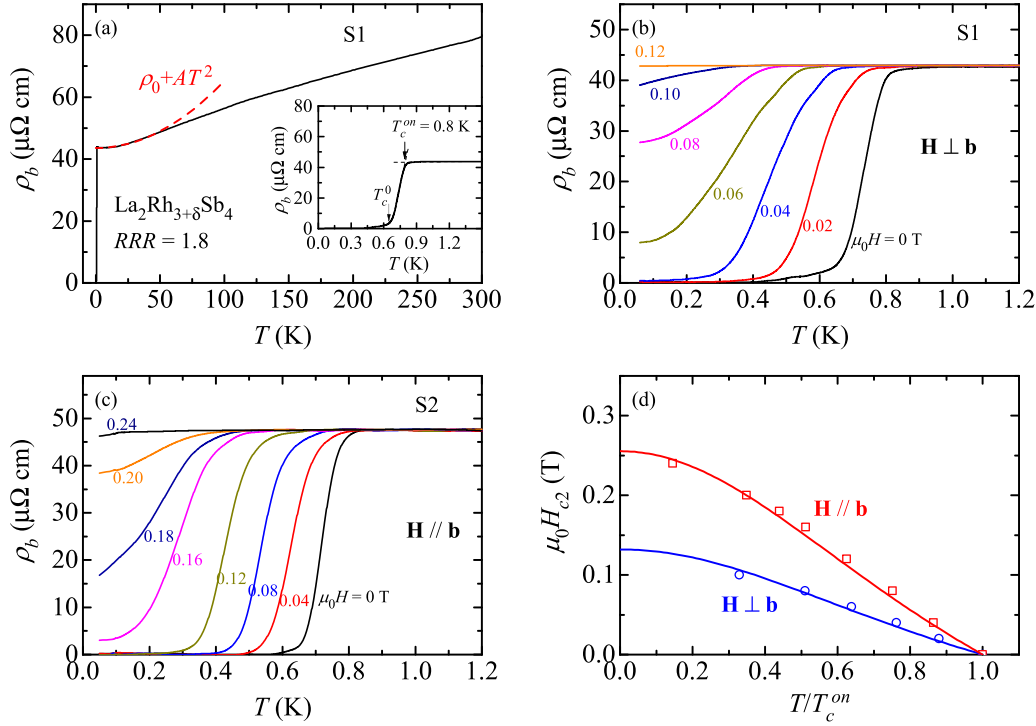


Figure 4. Electrical resistivity of $\text{La}_2\text{Rh}_{3+\delta}\text{Sb}_4$. (a) $\rho_b(T)$ profile showing superconducting transition with $T_c^{\text{on}} = 0.8 \text{ K}$ and $T_c^0 = 0.65 \text{ K}$. Figures (b) and (c) for $\rho_b(T)$ measured under magnetic field $\mathbf{H} \perp \mathbf{b}$ and $\mathbf{H} \parallel \mathbf{b}$, respectively. (d) Temperature dependent upper critical field $\mu_0 H_{c2}(T)$; the solid lines are fits to Ginzburg–Landau law.

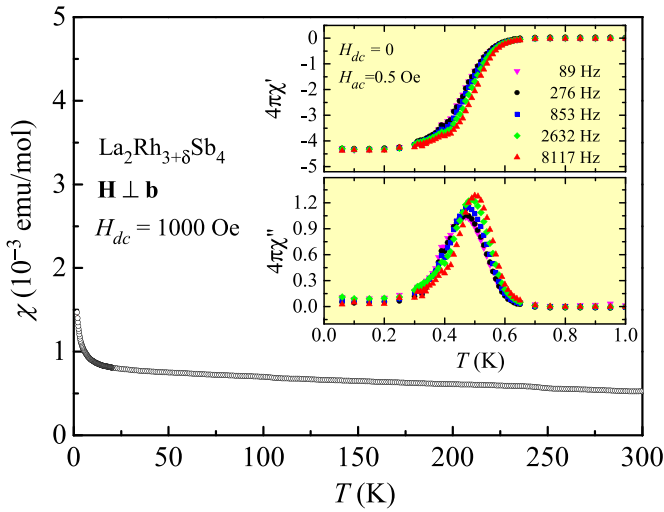


Figure 5. Temperature dependence of DC magnetic susceptibility for field perpendicular to \mathbf{b} . The insets present real (χ') and imaginary (χ'') parts of AC susceptibility as functions of T , measured at various frequencies.

are summarized in figure 6. At 200 K, the total specific heat C is about $206 \text{ J mol}^{-1}\cdot\text{K}$, close to the classic limit $3NR = 224.5 \text{ J mol}^{-1}\cdot\text{K}$ given by Dulong–Petit’s law [28], where $N = 9$ is the number of atoms in a formula unit of stoichiometric $\text{La}_2\text{Rh}_3\text{Sb}_4$, and $R = 8.314 \text{ J mol}^{-1}\cdot\text{K}$ is the ideal gas constant. The low temperature specific heat conforms to $C(T) = \gamma_n T + \beta T^3$, where the first and second terms are contributions from electrons (C_{el}) and phonons (C_{ph}). This is better expressed by the C/T vs. T^2 plot inset to figure 6.

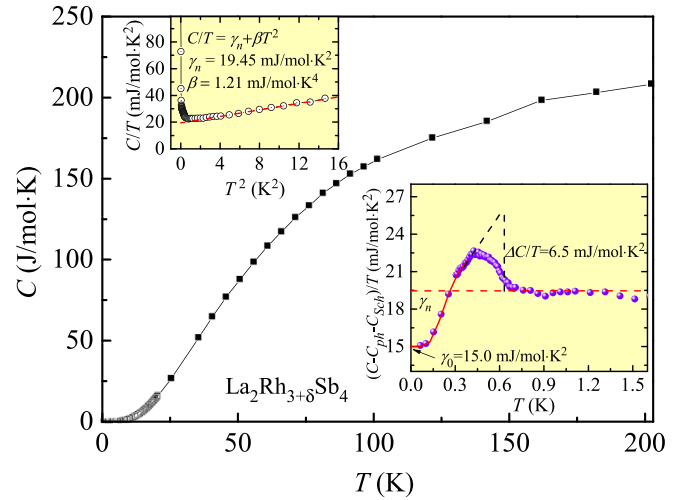


Figure 6. Temperature dependent specific heat (C) of $\text{La}_2\text{Rh}_{3+\delta}\text{Sb}_4$. The left inset shows a plot of C/T vs. T^2 in the low temperature range. The upturn of C/T for $T \rightarrow 0$ arises from the nuclear Schottky anomaly. The bottom inset, $(C - C_{\text{ph}} - C_{\text{Sch}})/T$ as a function of T , displays the jump due to SC transition $\Delta C/T|_{T_c} = 6.5 \text{ mJ mol}^{-1}\cdot\text{K}^2$.

This fit leads to the normal-state Sommerfeld coefficient $\gamma_n = 19.45 \text{ mJ mol}^{-1}\cdot\text{K}^2$, and $\beta = 1.21 \text{ mJ mol}^{-1}\cdot\text{K}^4$, and enables us to estimate the Debye temperature, $\Theta_D = (\frac{12\pi^4 NR}{5\beta})^{1/3} = 244 \text{ K}$. Note that the rapid increase of C/T for $T \rightarrow 0$ shown in the upper inset of figure 6 arises from the nuclear Schottky anomaly (C_{Sch}) and can be properly subtracted by fitting C_{Sch} to a $1/T^2$ law [29]. We then obtain C_{el} by subtracting both C_{ph}

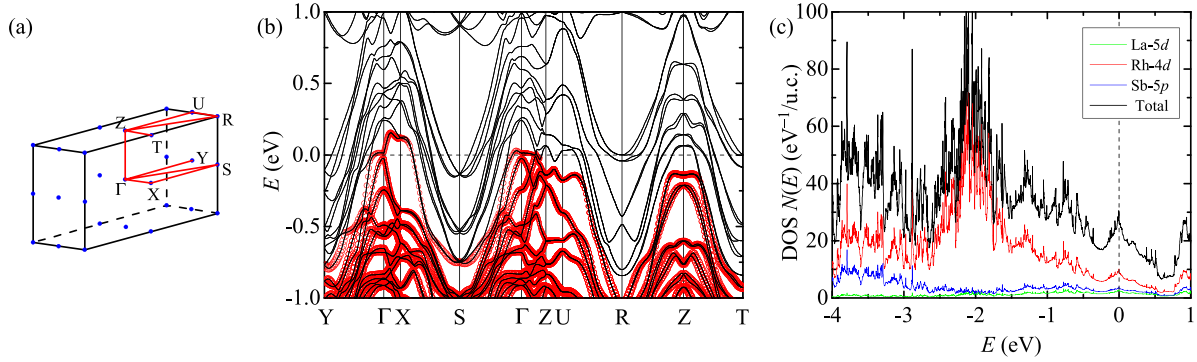


Figure 7. First-principles electronic structure of $\text{La}_2\text{Rh}_3\text{Sb}_4$. (a) Sketch of Brillouin zone. (b) Band structure where the size of the red and blue circles represent the weight of Rh-4d and Sb-5p orbitals, respectively. (c) Enlarged band structure along Y- Γ -Z paths to show the semi-flat feature near Γ . (d) Density of states. For pristine $\text{La}_2\text{Rh}_3\text{Sb}_4$, Fermi level likely sits at a van-Hove singularity where $N(E)$ peaks.

and C_{Sch} from the total $C(T)$, as shown in the lower inset to figure 6. The anomaly in specific heat due to the SC transition now can be clearly seen near 0.65 K, and the jump of specific heat at T_c is estimated $\Delta C/T|_{T_c} = 6.5 \text{ mJ mol}^{-1} \cdot \text{K}^2$. Below T_c , the electronic specific heat consists of two parts, viz. $C_{\text{el}}(T) = \gamma_0 T + C_{\text{sc}}(T)$, where γ_0 is the residual Sommerfeld coefficient, and C_{sc} describes the superconducting part of specific heat. We find that C_{sc} agrees well to the s -wave model [30], viz. $C_{\text{sc}}/T \propto T^{-5/2} \exp(-\Delta_0/T)$, in which Δ_0 characterizes the superconducting gap. This fit gives rise to $\gamma_0 = 15.0 \text{ mJ mol}^{-1} \cdot \text{K}^2$ and $\Delta_0 = 1.1 \text{ K}$. This manifests that only $\sim 23\%$ $[= (\gamma_n - \gamma_0)/\gamma_n]$ of the DOS at Fermi energy are gapped out due to the SC transition. One possible reason for this is the multi-band effect, (see figure 7), as Cooper pairs probably form only in some specific bands. Similar observation has been found in other multi-band superconductors, like PrNiAsO [31]. An alternative possibility could be due to some non-superconducting fraction. It is difficult to rule out this possibility only from the present data. Microscopic and local measurements like nuclear magnetic resonance, scanning tunneling microscope, and angle-resolved photoemission spectroscopy may be useful to clarify this issue. The analysis of specific heat further leads to two important ratios, $\frac{\Delta C}{(\gamma_n - \gamma_0)T_c} = 1.46$ and $\Delta_0/T_c = 1.69$. These values respectively are close to 1.43 and 1.76 as predicted by the Bardeen–Cooper–Schrieffer (BCS) theory [32, 33]. $\text{La}_2\text{Rh}_{3+\delta}\text{Sb}_4$, therefore, is probably an s -wave superconductor.

3.3. Electronic structure

The fully optimized lattice constants of *pristine* $\text{La}_2\text{Rh}_3\text{Sb}_4$ in DFT calculations are $a = 16.3862 \text{ \AA}$, $b = 4.6195 \text{ \AA}$, and $c = 11.0796 \text{ \AA}$. Compared to the experimental results, they are slightly increased, but all are within 3% error limit of the PBE functional, suggesting the validity of our calculations. Moreover, all relaxed internal coordinates are also accurate within 1% of the experimental values. Usually, such pronounced accuracy in plain DFT calculations is a hint of weak correlation of the compound.

We show the calculated band structure and DOS in figure 7. The electronic DOS near the Fermi level are dominated by Rh-4d and Sb-5p orbitals. The La-5d orbitals have only negligible contribution. The La-4f states are approximately 2 eV above the Fermi level and are irrelevant. Since the crystal structure contains inversion center, the spin degeneracy is preserved with SOC considered. As the crystal structure of the compound contains four formula units of $\text{La}_2\text{Rh}_3\text{Sb}_4$, its band structure is quite complicated too. There are as many as 12 doubly degenerate bands crossing the Fermi level, thus giving rise to 12 doubly degenerate Fermi surface sheets. Around Γ , semi-flat bands appear along Γ -Y and Γ -Z, seeing figure 7(c). As a result, a small DOS peak appear at the Fermi level in the pristine compound. These semi-flat bands may be related to reduced dimensionality in certain directions, as two of these bands do not cross the Fermi level along U-R and Z-T. Therefore, the DOS peak at E_F in the pristine $\text{La}_2\text{Rh}_3\text{Sb}_4$ may be interpreted as van-Hove singularity like, and yields a large $N(E_F) = 7.31 \text{ states/(f.u.} \cdot \text{eV)}$, or equivalently $\gamma_{\text{calc}} = 17.24 \text{ mJ mol}^{-1} \cdot \text{K}^2$. Compared to experimental value assuming $\gamma_n = \gamma_{\text{calc}}(1 + \lambda_{\text{elph}})$, we obtain a small electron–phonon coupling constant $\lambda_{\text{elph}} = 0.12$, which cannot account for the observed T_c . Alternatively, if we take the inter-site Rh4 impurities as charge dopants, we can estimate the amount of electron doping to be about 1 electron/unit cell [34]. Employing the rigid band approximation, the DOS at the Fermi level is found to be $N(E_F) = 6.0 \text{ states/(f.u.} \cdot \text{eV)}$, or equivalently $\gamma_{\text{calc}} = 14.14 \text{ mJ mol}^{-1} \cdot \text{K}^2$ for the doped system. Thus, the electron–phonon coupling constant of the $\text{La}_2\text{Rh}_{3+\delta}\text{Sb}_4$ can be estimated to be $\lambda_{\text{elph}} = 0.375$. T_c can be estimated according to the McMillan equation in the weak electron–phonon coupling regime [35],

$$T_c = \frac{\Theta_D}{1.45} \exp \left[-\frac{1.04(1 + \lambda_{\text{elph}})}{\lambda_{\text{elph}} - \mu^*(1 + 0.62\lambda_{\text{elph}})} \right], \quad (1)$$

where μ^* is Coulomb pseudopotential. This yields $T_c = 0.6 \text{ K}$, assuming a commonly used value $\mu^* = 0.10$ [36]. The nice agreement signals BCS weak-coupling scenario and conventional electron–phonon coupled pairing mechanism.

3.4. Discussion added

Some additional questions may have been invoked by this work. (a) It is still unknown how the pristine compound $\text{La}_2\text{Rh}_3\text{Sb}_4$ behave at low temperature, and whether and how SC depends on the Rh4 concentration δ . Since stoichiometric $\text{La}_2\text{Rh}_3\text{Sb}_4$ sits at the van Hove singularity, and the RRR may also be enhanced with less disorder, one might expect a higher T_c , assuming the electron–phonon coupling constant retains. However, this really depends. (b) According to what we have known from $\text{La}_2\text{Rh}_{3+\delta}\text{Sb}_4$ and $\text{Ce}_2\text{Rh}_{3+\delta}\text{Sb}_4$ [20], the values of δ both are close to 1/8. It will be interesting to investigate whether these Rh dopants form a specific order (e.g. the famous ‘1/8 anomaly’ in the high T_c cuprate $\text{La}_{1.875}\text{Ba}_{0.125}\text{CuO}_4$ [37]). In recent years, many antimonide superconductors have been found to be in close relation with charge order, e.g. CsV_3Sb_5 [38], IrSb [39, 40]. This remains an open issue in $\text{La}_2\text{Rh}_{3+\delta}\text{Sb}_4$. (c) Our work may also imply that the broad $\text{Ln}_2\text{Tm}_{3+\delta}\text{Sb}_4$ family may host new quantum material bases where new superconductors, quantum magnetism (note that geometrical frustration probably exists due to the triangular Ln sublattice), Kondo effect and other electronic correlation effects could be found. To address these issues, more investigations are needed in the future.

4. Conclusion

We successfully synthesized a new ternary rhodium-antimonide $\text{La}_2\text{Rh}_{3+\delta}\text{Sb}_4$ by a Bi-flux method. The compound crystallizes in the orthorhombic $\text{Pr}_2\text{Ir}_3\text{Sb}_4$ -like structure with redundant Rh acting as charge dopant. The refined crystal-line structure has been determined by single-crystal XRD and STEM. First-principles band structure calculations point out that it is a multi-band metal with a van-Hove singularity like feature close to the Fermi level. Ultra-low temperature resistivity, magnetic susceptibility, and specific heat measurements unveil it as a candidate of weak-coupling s -wave type-II superconductor.

Acknowledgments

This work was supported by the open research fund of Songshan Lake Materials Laboratory (2022SLABFN27), NSF of China (Grants Nos. 12004270, 51861135104, 11574097, 12204298, 12274364 and 11874137), the Fundamental Research Funds for the Central Universities of China (2019kfyXMBZ071), Guangdong Basic and Applied Basic Research Foundation (2019A1515110517), and the Pioneer and Leading Goose R&D Program of Zhejiang (2022SDXHDX0005).

ORCID iD

Yongkang Luo  <https://orcid.org/0000-0002-6098-5767>

References

- [1] Perry R S, Baumberger F, Balicas L, Kikugawa N, Ingle N J C, Rost A, Mercure J F, Maeno Y, Shen Z X and Mackenzie A P 2006 Sr_2RhO_4 : a new, clean correlated electron metal *New. J. Phys.* **8** 175
- [2] Luo Y K *et al* 2013 Li_2RhO_3 : a spin-glassy relativistic Mott insulator *Phys. Rev. B* **87** 161121
- [3] Movshovich R, Graf T, Mandrus D, Thompson J D, Smith J L and Fisk Z 1996 Superconductivity in heavy-fermion CeRh_2Si_2 *Phys. Rev. B* **53** 8241–4
- [4] Hegger H, Petrovic C, Moshopoulou E G, Hundley M F, Sarrao J L, Fisk Z and Thompson J D 2000 Pressure-induced superconductivity in quasi-2D CeRhIn_5 *Phys. Rev. Lett.* **84** 4986–9
- [5] Wastin F, Boulet P, Rebizant J, Colineau E and Lander G H 2003 Advances in the preparation and characterization of transuranium systems *J. Phys.: Condens. Matter* **15** S2279–85
- [6] Aoki D, Huxley A, Ressouche E, Braithwaite D, Flouquet J, Brison J-P, Lhotel E and Paulsen C 2001 Coexistence of superconductivity and ferromagnetism in URhGe *Nature* **413** 613–6
- [7] Khim S *et al* 2021 Field-induced transition within the superconducting state of CeRh_2As_2 *Science* **373** 1012–6
- [8] Kibune M *et al* 2022 Observation of antiferromagnetic order as odd-parity multipoles inside the superconducting phase in CeRh_2As_2 *Phys. Rev. Lett.* **128** 057002
- [9] Kumigashira H, Takahashi T, Yoshii S and Kasaya M 2001 Hybridized nature of pseudogap in Kondo insulators CeRhSb and CeRhAs *Phys. Rev. Lett.* **87** 067206
- [10] Gegenwart P, Custers J, Geibel C, Neumaier K, Tayama T, Tenya K, Trovarelli O and Steglich F 2002 Magnetic-field induced quantum critical point in YbRh_2Si_2 *Phys. Rev. Lett.* **89** 056402
- [11] Shen B *et al* 2020 Strange-metal behaviour in a pure ferromagnetic Kondo lattice *Nature* **579** 51–55
- [12] Onimaru T, Nagasawa N, Matsumoto K T, Wakiya K, Umeo K, Kittaka S, Sakakibara T, Matsushita Y and Takabatake T 2012 Simultaneous superconducting and antiferroquadrupolar transitions in $\text{PrRh}_2\text{Zn}_{20}$ *Phys. Rev. B* **86** 184426
- [13] Hofmann W K and Jeitschko W 1988 Ternary pnictides $\text{MNi}_{2-x}\text{Pn}_2$ ($M = \text{Sr}$ and rare earth metals, $\text{Pn} = \text{Sb}, \text{Bi}$) with defect CaBe_2Ge_2 and defect ThCr_2Si_2 structures *J. Less-Common Met.* **138** 313–22
- [14] Cava R J, Ramirez A P, Takagi H, Krajewski J J and Peck Jr W E 1993 Physical properties of some ternary Ce intermetallics with the transition metals Ni and Pd *J. Magn. Mater.* **128** 124–8
- [15] Yang X X, Lu Y M, Zhou S K, Mao S Y, Mi J X, Man Z Y and Zhao J T 2005 $\text{RCu}_{1+x}\text{Sb}_2$ ($R = \text{La}, \text{Ce}, \text{Pr}, \text{Nd}, \text{Sm}, \text{Gd}, \text{Tb}, \text{Dy}, \text{Ho}$ and Y) phases with defect CaBe_2Ge_2 -type structure *Mater. Sci. Forum* **475–479** 861–4
- [16] Luo Y *et al* 2012 Magnetism and crystalline electric field effect in ThCr_2Si_2 -type CeNi_2As_2 *Phys. Rev. B* **86** 245130
- [17] Luo Y, Ronning F, Wakeham N, Lu X, Park T, Xu Z-A and Thompson J D 2015 Pressure-tuned quantum criticality in the antiferromagnetic Kondo semimetal $\text{CeNi}_{2-\delta}\text{As}_2$ *Proc. Natl Acad. Sci. USA* **112** 13520–4
- [18] Schäfer K, Hermes W, Rodewald U C, Hoffmann R-D and Pöttgen R 2011 Ternary antimonides $\text{RE}_2\text{Ir}_3\text{Sb}_4$ ($\text{RE} = \text{La}, \text{Ce}, \text{Pr}, \text{Nd}$) *Z. Naturforsch. B* **66** 777–83

- [19] Cardoso-Gil R, Caroca-Canales N, Budnyk S and Schnelle W 2011 Crystal structure, chemical bonding and magnetic properties of the new antimonides $\text{Ce}_2\text{Ir}_3\text{Sb}_4$, $\text{La}_2\text{Ir}_3\text{Sb}_4$ and $\text{Ce}_2\text{Rh}_3\text{Sb}_4$ *Z. Kristallogr.* **226** 657–66
- [20] Cheng K Q and Luo Y K in preparation
- [21] Kresse G and Hafner J 1993 *Ab initio* molecular dynamics for liquid metals *Phys. Rev. B* **47** 558–61
- [22] Perdew J P, Burke K and Ernzerhof M 1996 Generalized gradient approximation made simple *Phys. Rev. Lett.* **77** 3865–8
- [23] Blöchl P E 1994 Projector augmented-wave method *Phys. Rev. B* **50** 17953–79
- [24] Kresse G and Joubert D 1999 From ultrasoft pseudopotentials to the projector augmented-wave method *Phys. Rev. B* **59** 1758–75
- [25] Ginzburg V L and Landau L D 1950 On the theory of superconductivity *Zh. Eksp. Teor. Fiz.* **20** 1064
- [26] Clogston A M 1962 Upper limit for the critical field in hard superconductors *Phys. Rev. Lett.* **9** 266–7
- [27] Chandrasekhar B S 1962 A note on the maximum critical field of high-field superconductors *Appl. Phys. Lett.* **1** 7–8
- [28] Ashcroft N W and Mermin N D 1976 *Solid State Physics* (Philadelphia, PA: Harcourt College Publishers)
- [29] Movshovich R, Yatskar A, Hundley M F, Canfield P C and Beyermann W P 1999 Magnetic-field dependence of the low-temperature specific heat in PrInAg_2 : support for a nonmagnetic heavy-fermion ground state *Phys. Rev. B* **59** R6601–3
- [30] Taylor O J, Carrington A and Schlueter J A 2007 Specific-heat measurements of the gap structure of the organic superconductors $\kappa\text{-(ET)}_2\text{Cu}[\text{N}(\text{CN})_2]\text{Br}$ and $\kappa\text{-(ET)}_2\text{Cu}(\text{NCS})_2$ *Phys. Rev. Lett.* **99** 057001
- [31] Li Y K, Luo Y K, Li L, Chen B, Xu X F, Dai J H, Yang X J, Zhang L, Cao G H and Xu Z A 2014 Kramers non-magnetic superconductivity in LnNiAsO superconductors *J. Phys.: Condens. Matter* **26** 425701
- [32] Bardeen J, Cooper L N and Schrieffer J R 1957 Microscopic theory of superconductivity *Phys. Rev.* **106** 162–4
- [33] Bardeen J, Cooper L N and Schrieffer J R 1957 Theory of superconductivity *Phys. Rev.* **108** 1175–204
- [34] The Rh4 atom is assumed to be divalent in the calculation. Taking $Z = 4$ and dopant concentration $\delta = 1/8$ for simplicity, we get 1 electron/u.c. Therefore, the Fermi level is assumed to change by $\Delta E = 39$ meV given by $\int_0^{\Delta E} N(E)dE = 1$. $N(\Delta E) = 24 \text{ eV}^{-1}/\text{u.c.}$
- [35] McMillan W L 1968 Transition temperature of strong-coupled superconductors *Phys. Rev.* **167** 331–44
- [36] Mu G, Zhu X Y, Fang L, Shan L, Ren C and Wen H-H 2008 Nodal gap in Fe-based layered superconductor $\text{LaO}_{0.9}\text{F}_{0.1-\delta}\text{FeAs}$ probed by specific heat measurements *Chin. Phys. Lett.* **2** 2221–4
- [37] Moodenbaugh A R, Xu Y W, Suenaga M, Folkerts T J and Shelton R N 1988 Superconducting properties of $\text{La}_{2-x}\text{Ba}_x\text{CuO}_4$ *Phys. Rev. B* **38** 4596–9
- [38] Wang Q et al 2021 Charge density wave orders and enhanced superconductivity under pressure in the Kagome metal CsV_3Sb_5 *Adv. Mater.* **33** 2102813
- [39] Qi Y P et al 2021 Superconductivity from buckled-honeycomb-vacancy ordering *Sci. Bull.* **66** 327–31
- [40] Ying T P, Yu T X, Cheng E J, Li S Y, Deng J, Cui X R, Guo J G, Qi Y P, Chen X L and Hosono H 2021 Fermi surface nesting, vacancy ordering and the emergence of superconductivity in IrSb compounds (arXiv:2108.13704)